Materials Science & Engineering A 978 (2026) 151088

Contents lists available at ScienceDirect

Materials Science & Engineering A

journal homepage: www.elsevier.com/locate/msea

Influence of initial lattice misorientation on the global and local response during wedge nanoindentation of single-crystal tungsten

T.O. Fenercioğlu [a,b], M. Budnitzki [a,*], J. Wang [b], S. Sandfeld [a,c], R. Schwaiger [b,d]

[a] Institute for Advanced Simulations – Materials Data Science and Informatics (IAS-9), Forschungszentrum Jülich GmbH, Jülich, 52425, Germany
[b] Institute of Energy Materials and Devices - Microstructure and Properties of Materials (IMD-1), Forschungszentrum Jülich GmbH, Jülich, 52425, Germany
[c] Chair of Materials Data Science and Materials Informatics, Faculty 5 – Georesources and Materials Engineering, RWTH Aachen University, Aachen, 52056, Germany
[d] Chair of Energy Engineering Materials, Faculty 5 – Georesources and Materials Engineering, RWTH Aachen University, Aachen, 52056, Germany

ARTICLE INFO

Keywords:
Nanoindentation
Initial lattice misorientation
TKD
Crystal plasticity
Finite element method

ABSTRACT

This work investigates the effect of small initial lattice misorientations on wedge nanoindentation in body-centered-cubic single-crystal tungsten using crystal plasticity finite element modeling. The study focuses on the sensitivity of both global and local indentation responses to controlled rotations of the initial crystal frame about the specimen axes. In the model, the imposed perturbation represents a crystallographic offset at the onset of indentation, while the specimen geometry, contact conditions, and boundary conditions remain unchanged.

The simulations show that small initial lattice misorientations produce only minor changes in the global load–displacement response, but substantially modify the local deformation field beneath the wedge. In particular, the lattice-rotation field becomes increasingly asymmetric, and the spatial distribution of dominant slip activity changes depending on both the axis and the magnitude of the imposed misorientation. Rotations involving the loading-axis component generate the strongest asymmetry, whereas in-plane rotations primarily influence the sign and localization of the lattice-rotation pattern beneath the indenter. Consistent with this behavior, the asymmetry index increased from a residual value of approximately 0.012 in the aligned reference configuration to substantially larger values for misoriented crystals, despite only minor changes in the corresponding load–displacement response.

These results indicate that local observables, such as lattice rotation and slip activity, are significantly more sensitive to the initial crystallographic state than the global indentation curve alone. The study therefore provides a mechanics-based framework for interpreting wedge-indentation experiments and associated orientation-mapping measurements in anisotropic crystalline materials, with particular relevance to single-crystal tungsten.

1. Introduction

Nanoindentation is an established technique for characterizing the mechanical response of materials by pressing a sharp indenter into the surface while continuously recording the applied load and displacement. From these measurements, properties such as hardness and elastic modulus can be extracted [1]. Due to the localized nature of the deformation zone, which often remains confined within individual grains, nanoindentation enables the measurement of orientation-dependent mechanical responses that are not easily accessible through conventional testing methods.

In crystalline metals, the mechanical response is significantly influenced by crystallographic orientation and the activity of specific slip systems. Because nanoindentation probes deformation at the scale of individual grains or subgrains, it is particularly effective for studying anisotropy in single crystals or textured polycrystalline materials, where bulk tests average out such effects. It also facilitates the analysis of size effects, strain gradients, and geometrically necessary dislocation (GND) densities [2,3]. These advantages are complemented by low material consumption and relatively simple sample preparation.

The load–displacement curve obtained during nanoindentation forms the basis for evaluating elastic modulus and hardness. The widely used Oliver–Pharr method [4] derives these properties from the curve's unloading segment, while accounting for contact area and elastic recovery. Further improvements to contact mechanics and area

* Corresponding author.
E-mail address: m.budnitzki@fz-juelich.de (M. Budnitzki).

https://doi.org/10.1016/j.msea.2026.151088
Received 7 July 2026; Received in revised form 4 September 2026; Accepted 13 September 2026
Available online 23 September 2026
0921-5093/© 2026 The Authors. Published by Elsevier B.V. This is an open access article under the CC BY license (http://creativecommons.org/licenses/by/4.0/).
Open access funding enabled and organized by Projekt DEAL.

function calibration, including tip shape deviations, have enhanced the precision of these measurements [5].

However, inconsistencies in measured properties across nominally similar samples have raised questions about the interpretation of nanoindentation results, especially for orientation-sensitive materials. One important source of variability is geometric sample misalignment, defined as the angular deviation between the sample surface normal and the indenter axis. Pelletier et al. [6] identified two types of such misalignment: (i) misalignment arising from sample preparation and mounting, and (ii) misalignment caused by imperfections in the indenter assembly. These effects alter the contact conditions and can lead to variations in load–displacement behavior, particularly for anisotropic materials and non-axisymmetric indenters such as the flat punch [7,8]. Analytical corrections for these geometric effects have been proposed for conical and pyramidal indenters [9].

In single-crystal materials, an additional source of variability arises from the initial crystallographic orientation relative to the specimen reference frame. In particular, the surface normal may deviate slightly from an intended low-index crystal direction, resulting in a small initial lattice misorientation at the onset of indentation. Even when the nominal specimen geometry and indenter alignment are unchanged, such crystallographic offsets can modify the local deformation response. Despite its importance, this form of initial crystallographic offset has received comparatively little attention in the literature, and its mechanistic implications remain insufficiently explored.

Recent experimental work by Wang et al. [3] examined size-dependent wedge indentation in single-crystal tungsten using combined nanoindentation and transmission Kikuchi diffraction (TKD). A pronounced asymmetry was observed in the subsurface lattice-rotation field beneath the indenter (see Fig. 1), with two distinct sectors separated by sharp orientation gradients inclined to the loading axis. In the original study, lattice rotation was reported through the evolution of three Euler-angle components. The present work focuses on the component exhibiting the strongest rotation signature, while the remaining components showed comparatively small variations. These observations indicate a strongly heterogeneous local deformation pattern beneath the wedge and provide a useful experimental reference for assessing the influence of crystallographic orientation on the indentation response.

To address this question, the present study numerically investigates the influence of small initial lattice misorientations on wedge nanoindentation in body-centered-cubic single-crystal tungsten. A crystal plasticity finite element model is employed to simulate elastoplastic deformation at the slip-system level and to track the evolution of lattice rotation [10–12] during indentation. After calibration against the measured load–displacement response, the model is used to impose controlled rotations of the initial crystal frame about the specimen axes and to examine their influence on both global and local observables. In this way, the study aims to clarify the micromechanical origins of local deformation heterogeneity and to improve the interpretation of orientation-sensitive wedge-nanoindentation measurements.

The present study therefore provides a computational framework for linking experimentally observed subsurface lattice-rotation asymmetries with their underlying micromechanical origins in wedge indentation of single-crystal tungsten. By systematically varying the initial crystal orientation while keeping the specimen geometry and boundary conditions fixed, the analysis isolates the influence of initial lattice misorientation on the global load–displacement response, the lattice-rotation field, and the evolving slip activity. The results help explain why local orientation-sensitive measurements can display strong asymmetry even when the corresponding global indentation curves remain comparatively similar, and they provide a more reliable basis for interpreting wedge-indentation experiments in anisotropic crystalline materials.

2. Methodology

A crystal plasticity finite element framework is employed to simulate wedge nanoindentation in body-centered-cubic (BCC) single-crystal tungsten. The simulations provide both global load–displacement (P–h) curves and spatially resolved local fields, including lattice rotation and slip activity, which are compared with experimental nanoindentation and orientation-mapping observations. Because crystal plasticity during indentation is highly anisotropic and heterogeneous at the micron scale, a full-field CPFEM approach is used to resolve the evolution of local slip-system activity and lattice rotation with sufficient spatial resolution.

2.1. Crystal plasticity framework

Crystal plasticity finite element modeling (CPFEM) provides a physically based framework for simulating orientation-dependent deformation mechanisms in crystalline materials. Unlike isotropic or polycrystal-averaged constitutive models, CPFEM explicitly resolves slip on individual crystallographic systems and tracks the evolution of lattice orientation and hardening at each integration point. This makes it particularly well suited for analyzing the highly localized deformation fields that develop during nanoindentation.

The present work adopts the rate-dependent crystal plasticity model originally implemented by Huang [13] as a user-defined material subroutine (UMAT) in Abaqus/Standard [14]. The formulation builds on the finite-deformation crystal-plasticity framework established by Hill [15], Lee [16], Rice [17], and Hill and Rice [18], and provides a numerically robust basis for large-strain simulations of single crystals. The finite element analysis accounts for the nonlinear nature of the indentation problem, including material nonlinearity arising from the crystal-plasticity formulation, contact nonlinearity associated with the evolving indenter–surface interaction, and geometric nonlinearity due to finite displacements and rotations. The latter is treated in Abaqus/Standard by enabling the finite-displacement formulation through `NLGEOM=YES`.

2.2. Constitutive model and numerical implementation

The kinematic description is based on the multiplicative decomposition of the deformation gradient,

$$\mathbf{F} = \mathbf{F}_\mathrm{e}\mathbf{F}_\mathrm{p}\,, \tag{1}$$

where $\mathbf{F}_\mathrm{e}$ represents the elastic lattice distortion and $\mathbf{F}_\mathrm{p}$ accounts for plastic deformation due to crystallographic slip. The plastic velocity gradient is constructed from the sum of shear contributions on all active slip systems,

$$\mathbf{L}_\mathrm{p} = \sum_{\alpha=1}^{N} \dot{\gamma}^\alpha \mathbf{s}^\alpha \otimes \mathbf{m}^\alpha\,, \tag{2}$$

where $\dot{\gamma}^\alpha$ is the slip rate, and $\mathbf{s}^\alpha$ and $\mathbf{m}^\alpha$ denote the slip direction and slip-plane normal, respectively. The slip rate is assumed to follow a power-law relation,

$$\dot{\gamma}^\alpha = \dot{\gamma}_0 \left(\frac{|\tau^\alpha|}{\tau_c^\alpha} \right)^n \mathrm{sign}(\tau^\alpha)\,, \tag{3}$$

where $\dot{\gamma}_0$ is the reference slip rate, n is the rate-sensitivity exponent, and τ_c^α is the critical resolved shear stress (CRSS) on system α. The resolved shear stress τ^α on system α is computed from the Cauchy stress $\boldsymbol{\sigma}$ as

$$\tau^\alpha = \boldsymbol{\sigma} : (\mathbf{s}^\alpha \otimes \mathbf{m}^\alpha)\,. \tag{4}$$

The elastic constitutive response is expressed through the constitutive relation between the Green–Lagrange strain and the second Piola–Kirchhoff stress tensor,

$$\mathbf{T} = \frac{1}{2} C : (\mathbf{F}^{eT}\mathbf{F}^{e} - \mathbf{I}), \tag{5}$$

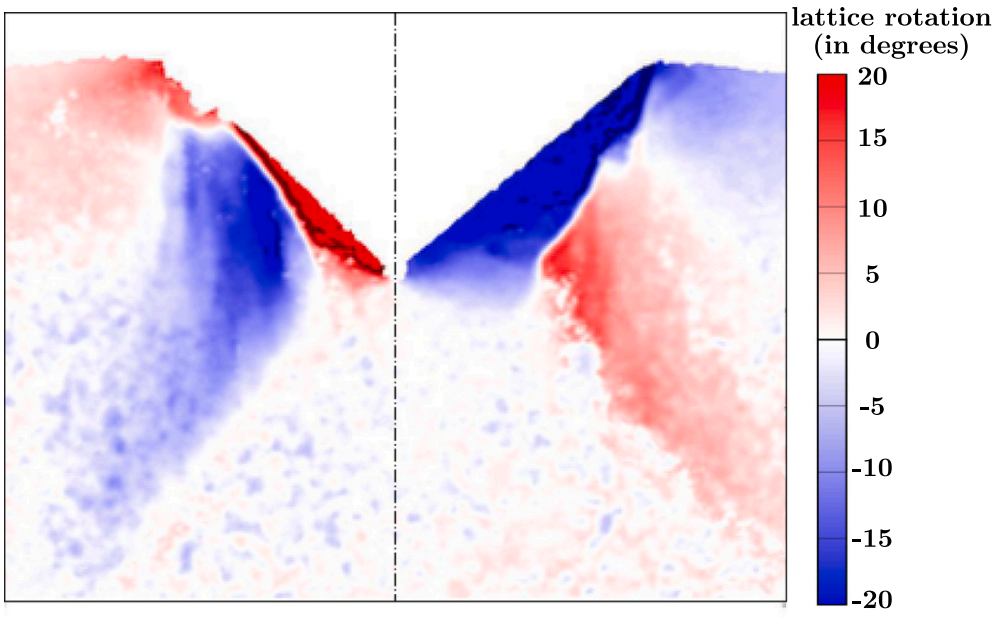

Fig. 1. Transmission Kikuchi diffraction (TKD) map showing the in-plane Euler-angle deviation beneath a wedge indent in single-crystal tungsten, adapted from [3]. Orientation gradients inclined to the loading axis divide the deformation zone into two asymmetric sectors, indicating a strongly heterogeneous deformation pattern beneath the indenter.

where C is the fourth-order stiffness tensor.

The evolution of the critical resolved shear stress (CRSS) τ_c^α on slip system α is governed by a rate-independent hardening law based on the formulation by [19]

$$\dot{\tau}_c^\alpha = \sum_{\beta=1}^{N} h_{\alpha\beta} \left| \dot{\gamma}^\beta \right| , \tag{6}$$

where $h_{\alpha\beta}$ denotes the hardening matrix describing both self and latent hardening interactions among slip systems. In the original model by Huang [13], the self-hardening component is given by

$$h_{\alpha\alpha} = h_0 \, \mathrm{sech}^2 \left(\left| \frac{h_0 \gamma^\alpha}{\tau_s - \tau_0} \right| \right) , \tag{7}$$

and the latent hardening terms are assumed to be proportional, i.e.,

$$h_{\alpha\beta} = q \cdot h_{\alpha\alpha} \quad (\alpha \neq \beta), \tag{8}$$

where γ^α is the accumulated slip on slip system α, h_0 is the initial hardening modulus, τ_s is the saturation stress, τ_0 is the initial CRSS, and q is a scalar latent hardening coefficient. The specific values adopted for the tungsten simulations are introduced in Section 3.1 and the final calibrated parameter set is summarized in Table 3.

Although the hardening evolution is evaluated independently for each slip system, Huang's original implementation defines the hardening parameters h_0, τ_s, and τ_0 as global scalars, shared uniformly across all systems. As such, the model does not support slip-system-dependent hardening parameters without modification of the UMAT. While this simplifies parameter calibration, it also limits the ability to represent crystallographically distinct hardening behavior. For the present application to high-purity single-crystal tungsten, this approximation is considered acceptable, since the dominant active systems are expected to exhibit similar hardening behavior and system-resolved calibration data are not available.

2.3. Initial lattice misorientation and lattice rotation export

We represent *initial lattice misorientation* as a rigid rotation of the crystal frame at every integration point using Bunge Euler angles $(\varphi_1, \phi, \varphi_2)$ with the Z–X′–Z″ convention [20]. Prescribed rotations are applied to emulate an intrinsic offset between the surface normal and a low-index crystal direction. Unless otherwise noted, positive angles follow the right-hand rule about the $+X, +Y, +Z$ axes.

Let $\mathbf{R}^0_{\mathrm{crys}}$ be the initial lattice-to-sample rotation (orientation) at $t = 0$. A user-specified lattice misorientation $\theta = (\theta_x, \theta_y, \theta_z)$ about the global axes is introduced via

$$\mathbf{R}_{\mathrm{mis}}(\theta) = \mathbf{R}_z(\theta_z)\,\mathbf{R}_y(\theta_y)\,\mathbf{R}_x(\theta_x), \qquad \mathbf{R}^0 = \mathbf{R}_{\mathrm{mis}}(\theta)\,\mathbf{R}^0_{\mathrm{crys}}. \tag{9}$$

Here $\mathbf{R}_\alpha(\cdot)$ are the standard right-handed rotation matrices about axis $\alpha \in \{x, y, z\}$. Eq. (9) rotates the crystal lattice relative to the sample frame while leaving the boundary-value problem geometrically unchanged, thereby isolating the effect of initial lattice misorientation.

During the simulation, the current lattice frame is reconstructed at each increment from the updated slip-system directions. For a slip system α with unit slip direction $\mathbf{s}^\alpha$ and unit slip-plane normal $\mathbf{m}^\alpha$, we define the transverse unit vector $\mathbf{t}^\alpha = \mathbf{m}^\alpha \times \mathbf{s}^\alpha$ and assemble the column-wise triad

$$\mathbf{Q}^\alpha = \left[\mathbf{s}^\alpha \;\; \mathbf{t}^\alpha \;\; \mathbf{m}^\alpha \right]. \tag{10}$$

To suppress round-off drift, $\mathbf{Q}^\alpha$ is re-orthonormalized if needed. The resulting lattice rotation tensor $\mathbf{R}$ is taken as the closest proper orthogonal matrix to $\mathbf{Q}^\alpha$.

At the end of each increment, we convert $\mathbf{R}$ to Bunge Euler angles $(\varphi_1, \phi, \varphi_2)$ and write them to file for direct comparison with EBSD/TKD maps. Using the standard Z–X′–Z″ convention, one convenient extraction is

$$\phi = \arccos\left(R_{33}\right), \;\; \varphi_1 = \mathrm{atan2}\left(R_{31}, -R_{32}\right), \;\; \varphi_2 = \mathrm{atan2}\left(R_{13}, R_{23}\right) \tag{11}$$

with the usual safeguards for the $\sin\phi \approx 0$ (gimbal) case.[1] Alongside $(\varphi_1, \phi, \varphi_2)$, we export per-system shear rates $\dot{\gamma}^\alpha$ and accumulated slips γ^α, which we later use to build lattice-rotation maps and "slip-activity fingerprints".

[1] In the $\sin\phi \to 0$ limit we set $\varphi_2 = 0$ and solve for φ_1. The full algorithm with edge-case handling is provided in Appendix A.

2.4. Finite element setup

A three-dimensional CPFEM model of wedge nanoindentation is constructed in Abaqus/Standard. The domain contains the single-crystal tungsten sample and the diamond indenter, both meshed with C3D8 bricks (see Fig. 2). A single element layer is used in the out-of-plane direction to represent a plane-strain-type section of the wedge-indentation problem. This approximation is appropriate for the central region of a long wedge, where the geometry and loading are assumed to be uniform along the wedge length. The use of three-dimensional brick elements retains the full three-dimensional crystal-plasticity constitutive formulation and slip-system kinematics, while avoiding unnecessary discretization along the uniform out-of-plane direction.

Boundary conditions and loading. The bottom surface of the sample is fully fixed. The front and rear faces are constrained in the out-of-plane direction to approximate plane strain conditions, and the side faces are constrained in the Y direction. Indentation is imposed by prescribing a vertical displacement $h(t)$ in the Z direction at a reference point kinematically coupled using a multi-point constraint (MPC) to the indenter top surface, ensuring rigid-body motion of the indenter top. Unless otherwise noted, the maximum applied displacement is $h_{\max}$ = 2 μm; in calibration runs the experimentally measured displacement history (Appendix B) is used. The total reaction force at the reference point is recorded to construct the load–displacement ($P-h$) curve.

Contact and friction. Normal contact is modeled as "hard", while tangential contact is treated using a penalty formulation. Consistent with the parameter-sensitivity analysis (Section 3.2) and prior studies [21,22], the friction coefficient μ has negligible influence on the global response over typical ranges. Because very low μ can promote localized deformation and trigger element distortion, a value of $\mu = 0.3$ is adopted for stability and comparability.

Indenter properties. To capture finite stiffness effects, the indenter is modeled as an elastic diamond body with E_i = 1140 GPa and ν_i = 0.07; the tip radius is set to r = 0.1 μm to match the experimental configuration of Wang et al. [3].

Discretization and mesh convergence. The mesh is refined near the contact region with a minimum element size of 0.05 μ m; away from the contact zone a graded refinement triples the element size at each transition. The inner refined rectangle is approximately 1.7 μm×3.4 μm. The full model contains 8360 elements (6348 in the sample, 2012 in the indenter). Mesh convergence was verified: a further refinement to 0.02 μ m changed the maximum load by <2% but increased runtime from ∼2 h to nearly 24 h, so the 0.05 μ m mesh was selected as an accuracy–cost compromise.

Loading history. Because the CPFEM formulation is rate dependent, the indentation boundary condition is based on the experimentally measured displacement–time history rather than an idealized constant loading rate. The raw experimental signal is smoothed and fitted by a sixth-order polynomial to obtain a strictly monotonic indentation history and a stable analytical velocity function $v(t)$. Prescribing the velocity history instead of the direct displacement helps regularize the loading path and improves numerical convergence in the rate-dependent simulations. Further details of the data processing, polynomial fit, and comparison with constant-velocity loading are provided in Appendix B.

3. Simulation of indentation in Tungsten

We first quantify how modeling choices and constitutive parameters influence the key observables of wedge nanoindentation. To anchor the model, we calibrate the constitutive parameters against experimental $P-h$ response for single-crystal tungsten. Subsequently, we analyze how initial lattice misorientation influences wedge nanoindentation of single-crystal tungsten, considering both global ($P-h$ curves) and local (lattice-rotation and slip-activity) observables.

3.1. Tungsten

The present subsection summarizes the crystallographic structure and constitutive parameters used for single-crystal tungsten in the CPFEM simulations. Unless otherwise stated, the baseline material parameters are taken from [23] and [24]. These include the elastic constants C_{11} = 532.6 GPa, C_{12} = 204.9 GPa, and C_{44} = 163.1 GPa, together with the rate-sensitivity exponent n = 20, reference slip rate $\dot{\gamma}_0 = 10^{-4}$ s^{-1}, initial hardening modulus h_0 = 1350 MPa, saturation stress τ_s = 530 MPa, and initial critical resolved shear stress τ_0 = 210 MPa.

For the CPFEM simulations, the full anisotropic single-crystal elastic constants are retained. For the parameter sensitivity analysis, however, equivalent isotropic elastic parameters are introduced in order to vary the overall elastic stiffness in a controlled manner. To derive these equivalent isotropic parameters, the Voigt and Reuss bounds for the bulk and shear moduli are first calculated and then averaged using the Hill (Voigt–Reuss–Hill) scheme [25]. Here, the subscripts V and R denote the Voigt and Reuss estimates, respectively, with K_V and G_V representing the Voigt bulk and shear moduli and K_R and G_R the corresponding Reuss bulk and shear moduli. The Hill estimates, K_H and G_H, are obtained as the arithmetic means of the corresponding Voigt and Reuss values. For cubic crystals, these quantities are given by

$$K_V = K_R = K_H = \frac{C_{11}+2C_{12}}{3} = 314.13 \text{ GPa}, \tag{12}$$

$$\begin{aligned} G_V &= \tfrac{C_{11}-C_{12}+3C_{44}}{5} = 163.40 \text{ GPa}, \\ G_R &= \tfrac{5C_{44}(C_{11}-C_{12})}{4C_{44}+3(C_{11}-C_{12})} = 163.40 \text{ GPa}. \end{aligned} \tag{13}$$

The Hill-averaged shear modulus is therefore

$$G_H = \frac{G_V+G_R}{2} \approx 163.40 \text{ GPa}. \tag{14}$$

Using the standard isotropic relations, the corresponding Young's modulus and Poisson's ratio are computed as

$$E = \frac{9K_HG_H}{3K_H+G_H}, \qquad \nu = \frac{3K_H-2G_H}{2(3K_H+G_H)}, \tag{15}$$

Using these relations gives $E \approx 418$ GPa and $\nu \approx 0.278$. For the parameter sensitivity analysis, these values are rounded to E = 400 GPa and ν = 0.28 for convenience. A verification study was performed by comparing the load–displacement response obtained using the equivalent isotropic elastic properties with that obtained using the full anisotropic single-crystal elastic constants. The relative difference between the two responses was evaluated across the loading segment. The maximum pointwise difference was 1.49%, the average difference over the compared loading range was 0.52%, and the difference at the maximum-load condition was 0.31%. These small differences confirm that the equivalent isotropic approximation has only a minor influence on the global load–displacement response considered in the elastic-parameter sensitivity analysis. The full anisotropic elastic constants are retained in the calibrated simulations and in the subsequent misorientation analysis. The parameter E is then varied systematically, with ν held fixed, in order to assess the sensitivity of the lattice-rotation field to changes in the overall elastic stiffness.

Tungsten has a body-centered-cubic (BCC) crystal structure with three crystallographically available slip families: {110}⟨111⟩, {112}⟨111⟩, and {123}⟨111⟩. The first slip family, {110}⟨111⟩, is illustrated in Table 1, which summarizes the corresponding slip planes and slip directions used in the model definition.

3.2. Sensitivity to model parameters

The sensitivity study considers two parameter groups: (i) *modeling parameters*, namely the friction coefficient μ and the indenter tip radius r, and (ii) *constitutive parameters*, including the elastic constants

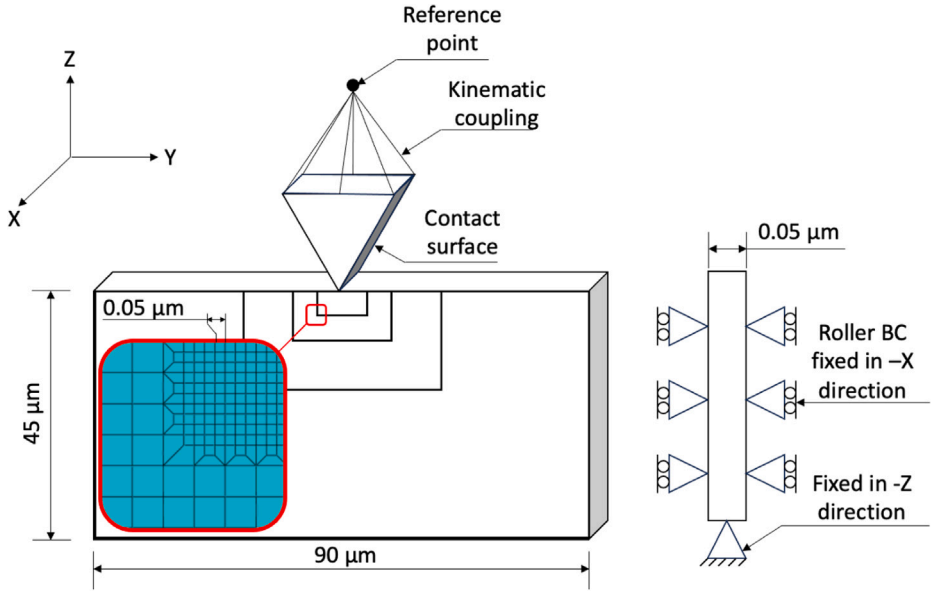

Fig. 2. Finite element model of wedge nanoindentation showing the indenter and sample geometry, boundary conditions, contact definition, and mesh refinement strategy. The displacement boundary condition is transferred from the reference point to the indenter top surface through kinematic coupling.

Table 1
Slip systems belonging to the first slip family, $\{110\}\langle 111\rangle$, in BCC single-crystal tungsten. The slip planes are hatched and the slip directions are indicated by arrows. The numbering of the slip systems corresponds to the labels used in the slip-activity maps shown in Figs. 3, 9, and subsequent figures.

Slip system 1 $\{011\}\langle 1\bar{1}1\rangle$	Slip system 2 $\{011\}\langle 11\bar{1}\rangle$	Slip system 7 $\{0\bar{1}1\}\langle 111\rangle$	Slip system 8 $\{0\bar{1}1\}\langle \bar{1}11\rangle$
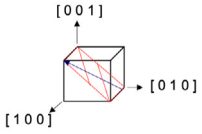	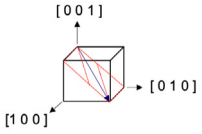	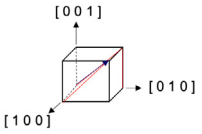	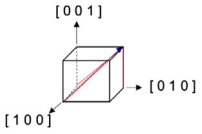
Slip system 3 $\{101\}\langle \bar{1}11\rangle$	Slip system 4 $\{101\}\langle 1\bar{1}1\rangle$	Slip system 9 $\{10\bar{1}\}\langle 111\rangle$	Slip system 10 $\{10\bar{1}\}\langle 1\bar{1}1\rangle$
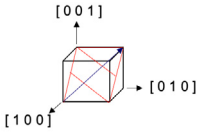	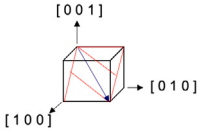	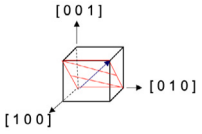	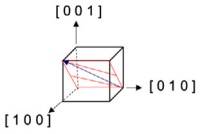
Slip system 5 $\{110\}\langle \bar{1}11\rangle$	Slip system 6 $\{110\}\langle 1\bar{1}1\rangle$	Slip system 11 $\{\bar{1}10\}\langle 111\rangle$	Slip system 12 $\{\bar{1}10\}\langle 11\bar{1}\rangle$
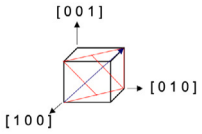	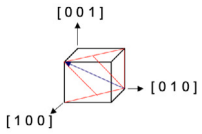	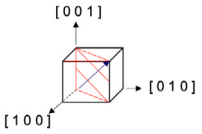	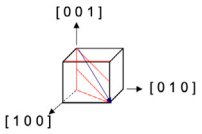

C_{11}, C_{12}, and C_{44}, the hardening parameters τ_0, h_0, and τ_s, the rate-sensitivity exponent n, the reference slip rate $\dot{\gamma}_0$, and the number of active slip families. Model responses are evaluated using four observables: the global P–h curve, the surface profile (pile-up or sink-in), the lattice-rotation field, and the slip-activity distribution. A parameter is classified as *sensitive* to a given observable when its variation produces a change exceeding 10% over the range considered. The results are summarized qualitatively in Table 2.

Modeling parameters. Within the present configuration, the friction coefficient μ has negligible influence on both global and local responses over the typical range $0.1 \leq \mu \leq 0.7$. Very low friction values ($\mu \lesssim 0.2$), however, promote localized deformation and element distortion; accordingly, $\mu = 0.3$ is adopted as a stable reference value. Indenter tip wear, represented by increasing the tip radius from $r = 0$ to 0.5 µm, increases $P_{\max}$ by approximately 15% while leaving the unloading slope, lattice-rotation patterns, and slip-activity fingerprints essentially unchanged.

Constitutive parameters. The slip-system numbers used in the activity maps correspond directly to the numbering given in Table 1. Fig. 3 illustrates the corresponding changes in dominant slip activity for

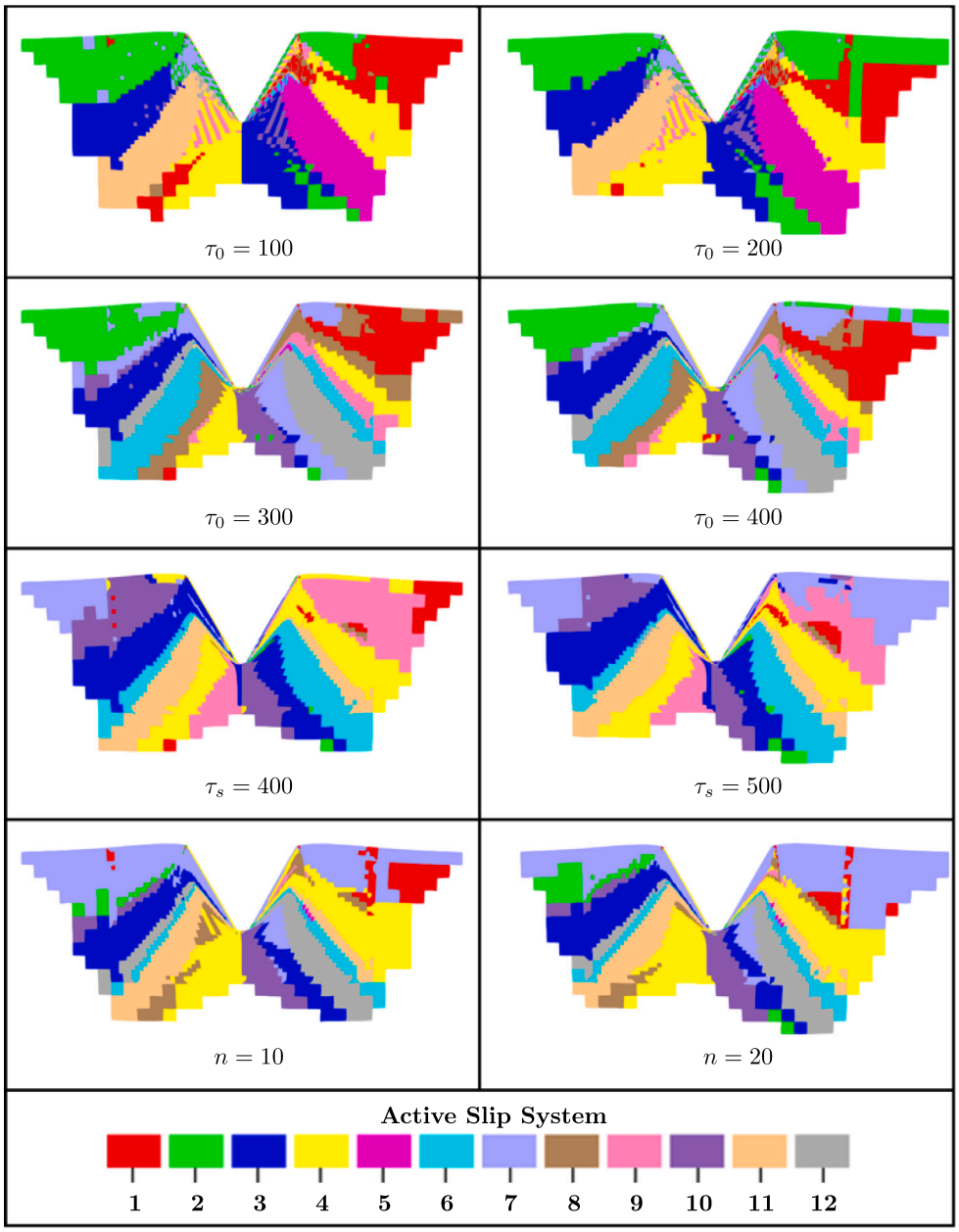

Fig. 3. Slip-system activity maps beneath the wedge indenter illustrating the sensitivity to selected constitutive parameters. The figure is organized into three blocks corresponding to variations in the initial critical resolved shear stress τ_0, the saturation stress τ_s, and the power-law exponent n. Colors denote the dominant slip system at the element centroid. Variations in τ_0 primarily affect slip-system competition and the emergence of dominant systems along the indenter shoulders; changes in τ_s are associated with the transition between pile-up and sink-in and with the stabilization of slip activity in the shoulder regions; and variations in n promote stronger localization and redistribute dominant slip activity between the indenter tip and shoulder regions. (For interpretation of the references to color in this figure legend, the reader is referred to the web version of this article.)

variations in the constitutive parameters τ_0, τ_s, and n. Variations in the initial critical resolved shear stress τ_0 primarily affect slip-system competition and the development of dominant systems along the indenter shoulders, while also influencing the spatial extent over which multiple slip systems coexist beneath the contact. Changes in τ_s are closely associated with the surface-profile transition between pile-up and sink-in and with the stabilization of dominant slip activity in the shoulder regions. In contrast, the rate-sensitivity exponent n has a stronger influence on the localization of plastic deformation, leading to pronounced redistribution of dominant slip activity between the indenter tip and shoulder regions. Increasing n promotes sharper localization near the tip and reduces the relative contribution of shoulder-dominated slip systems.

The corresponding influence of the constitutive parameters on the global load–displacement response is summarized in Fig. 4. Reducing the elastic modulus E (for example from 500 to 200 GPa) lowers both $P_{\max}$ and the unloading stiffness, with the sensitivity decreasing above approximately 300 GPa. The initial hardening modulus h_0 also has a strong influence on the global load–displacement response. By contrast, τ_0, τ_s, and n affect not only the global curve but also the local deformation fields beneath the indenter.

The number of active slip families has an especially strong effect on $P_{\max}$: allowing additional families softens the response by opening more slip directions (cf. Fig. 5(b)). For this reason, the subsequent calibration and misorientation analyses are performed using a reduced

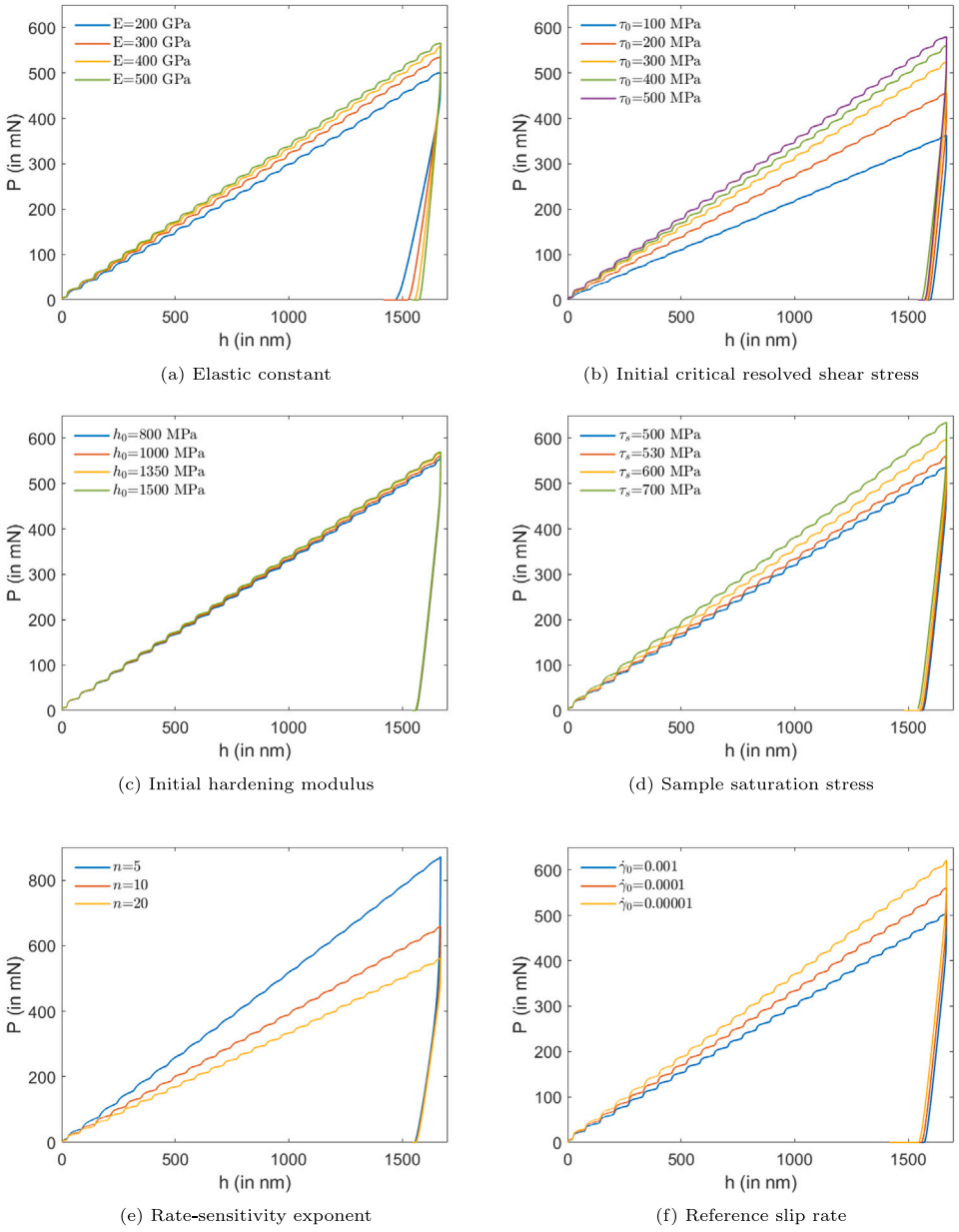

Fig. 4. Sensitivity of the load–displacement curve with respect to six constitutive model parameters (E, ICSS, IHM, SS, PHE, HC) in the wedge indentation model, shown in subfigures (a)–(f). Note that, at the end of the loading segment, a vertical drop in the load is observed in the curves while the indentation depth remains constant. This behavior arises from the hold period implemented at maximum indentation depth, during which the indenter is kept stationary to capture viscoplastic relaxation mechanisms.

single-family description, for which the response shows substantially higher sensitivity to the constitutive parameters.

3.3. Calibration based on load–displacement curves for W

We calibrate the constitutive parameters of the CPFEM model against the experimental load–displacement (P–h) response for single-crystal tungsten. Following a re-evaluation of the measurements, the loading segment is linearized over the range 700–1800 nm in order to reduce the influence of early-contact uncertainties and instrument-related effects [26]. The slope of this linearized segment, together with the experimental value of P_{max}, defines the target response for the simulations. The purpose of the linearization is not to approximate the complete experimental loading trajectory, but to establish a consistent reference for calibrating the finite element model. The initial nonlinear portion of the experimental P–h curve is excluded because it is expected to be strongly influenced by contact-related and experimental effects, including initial contact detection, tip rounding, local surface effects, instrument compliance, and possible small geometric misalignment. These contributions cannot be quantified independently in the present model and are therefore not considered a reliable basis for calibrating the crystal-plasticity material response.

The linearized target is constructed from the experimentally determined loading stiffness over the selected 700–1800 nm range while retaining the measured P_{max} (see Fig. 5(a)). As a consequence, the maximum indentation depth of the linearized curve is lower than

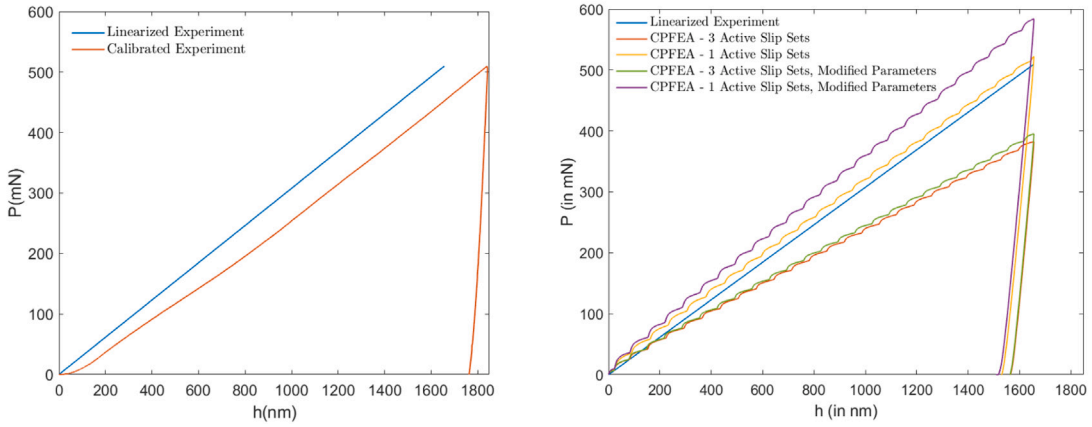

(a) Linearization of experimental results (b) Model Parameter Fitting

Fig. 5. Model fitting. (a) Linearization of the experimental load–displacement response obtained from the nanoindentation measurements. The range below approximately 700 nm shows a varying tangent due to initial contact effects and tip geometry; the segment between 700 and 1800 nm is therefore used for linearization, as indicated by the blue curve. (b) Calibration of the CPFEM response against the linearized experimental reference. Simulations with three active BCC slip families show a response that is too soft relative to the experimental curve, and varying the initial critical resolved shear stress and hardening modulus in that setting produces only limited changes in the response. Restricting plastic flow to the $\{110\}\langle 111\rangle$ family yields a substantially improved fit and markedly increases the sensitivity of the response to τ_0 and h_0, as illustrated by the yellow and purple curves. (For interpretation of the references to color in this figure legend, the reader is referred to the web version of this article.)

Table 2
Summary of parameter sensitivity in wedge-indentation simulations. "+" indicates a change greater than 10% in the listed output over the studied parameter range; "–" indicates a change below 10%.

Input/Output	$P-h$	Surface profile	Lattice rotation	Slip activity
Modeling parameters				
Friction coefficient μ	–	–	–	–
Tip radius r	+	–	–	–
Constitutive parameters				
Elastic constants C	+	–	–	–
Initial CRSS τ_0	+	+	+	+
Initial hardening h_0	+	–	–	–
Saturation stress τ_s	+	+	+	+
Power exponent n	+	+	+	+
Reference slip rate $\dot{\gamma}_0$	+	–	–	–
Active slip families	+	–	–	–

that of the original experimental curve. This limits direct quantitative comparison with the experiment in terms of absolute indentation depth, deformation-zone size, and local field magnitude. However, its influence on the conclusions of the present study is expected to be limited because the misorientation analysis is comparative, with all cases evaluated using the same calibrated reference model and loading conditions.

Because the crystal-plasticity formulation is rate sensitive, we prescribe the experimentally measured displacement–time history $h(t)$ rather than an idealized constant indentation velocity as the kinematic boundary condition at the indenter reference point. The corresponding velocity history is obtained by numerical differentiation of $h(t)$. Since the raw signal contains small non-monotonic segments, it is smoothed using moving averages prior to differentiation (Appendix B, Fig. B.12). This treatment considerably improves numerical stability without materially affecting the calibrated response; after recalibration with the corrected rate history, the resulting lattice-rotation fields and slip-activity patterns remain essentially unchanged.

The optimal parameter set $\hat{\boldsymbol{\eta}}$ is obtained by minimizing the squared error between the linearized experimental loading curve $P_{\mathrm{exp}}(h)$ and the simulated response $P_{\mathrm{sim}}(h;\boldsymbol{\eta})$:

$$\hat{\boldsymbol{\eta}} = \arg\min_{\boldsymbol{\eta}} J(\boldsymbol{\eta}), \tag{16}$$

with

$$J(\boldsymbol{\eta}) = \sum_{i=1}^{N} \left[P_{\mathrm{sim}}(h_i;\boldsymbol{\eta}) - P_{\mathrm{exp}}(h_i)\right]^2. \tag{17}$$

Using the full set of three BCC slip families, $\{110\}\langle 111\rangle$, $\{112\}\langle 111\rangle$, and $\{123\}\langle 111\rangle$, produces a response that remains too compliant relative to the experimental loading curve near $P_{\max}$. In this setting, varying the initial critical resolved shear stress τ_0 and the initial hardening modulus h_0 within physically reasonable bounds increases $P_{\max}$ by only approximately 3%, which is insufficient to reproduce the measured loading response. The corresponding model therefore lacks the parameter sensitivity required for a meaningful calibration under the present indentation conditions (see Fig. 5(b)).

For this reason, the subsequent analysis restricts plastic flow to the $\{110\}\langle 111\rangle$ family, which is consistent with the expected dominant slip response under the present room-temperature indentation conditions. Within this reduced formulation, the model shows substantially improved sensitivity to τ_0 and h_0, and good agreement with the linearized experimental P–h response is obtained. The final parameter set used in the subsequent misorientation study is summarized in Table 3. The elastic constants are retained from the literature, the rate-dependent parameters are kept at their baseline values, and the reduced $\{110\}\langle 111\rangle$ slip description is combined with fitted values of τ_0 and h_0 to reproduce the experimental response.

3.4. Effects of initial lattice misorientation

We now examine how small initial lattice misorientations modify both the global and local response during wedge nanoindentation of single-crystal tungsten within the CPFEM framework. The imposed misorientation is parameterized by the rotation vector $\boldsymbol{\theta} = (\theta_x, \theta_y, \theta_z)$ about the global axes, with positive angles defined by the right-hand rule (cf. Section 2.3). Unless stated otherwise, all responses are compared at the maximum indentation depth $h_{\max}$ and plotted using a common axis range and color scale to enable direct comparison across cases. The

Table 3
Calibrated constitutive parameters for single-crystal tungsten used in the initial lattice misorientation study. Elastic constants are in Voigt notation.

Parameter	Symbol	Value	Notes
Elastic constants	(C_{11}, C_{12}, C_{44})	(532.6, 204.9, 163.1) GPa	Liu et al. [23]
Rate exponent	n	20	Volz [24]
Reference slip rate	$\dot{\gamma}_0$	10^{-4} s^{-1}	Volz [24]
Initial CRSS	τ_0	400 MPa	Fitted
Initial hardening modulus	h_0	1000 MPa	Fitted
Saturation stress	τ_s	530 MPa	Volz [24]
Active slip family	–	$\{110\}\langle 111\rangle$	Consistent with RT deformation

experimental configuration, with the indentation surface normal parallel to [001] and the wedge direction aligned with [110], i.e. (001)[110], is adopted as the reference crystal orientation in the finite element model. This corresponds to an $\mathbf{R}^0_{\text{crys}}$, which can be expressed using the Bunge convention as $(\varphi_1^0, \phi^0, \varphi_2^0) = (45°, 0°, 0°)$. As detailed in Section 2.3, the prescribed angles $(\theta_x, \theta_y, \theta_z)$ represent rotations of the crystal frame relative to this reference orientation and should therefore be interpreted as imposed misorientations, not as Bunge Euler angles. The resulting lattice orientations are subsequently expressed using the Bunge convention for comparison with the TKD measurements.

The analysis proceeds in three steps. First, the aligned case (0°, 0°, 0°) is used to establish a baseline, and the simulated P–h response together with the lattice-rotation field is compared with prior observations. Second, single-axis misorientations are introduced to separate the roles of the X-, Y-, and Z-components; this reveals symmetry breaking and, in some cases, a sign inversion of the lattice rotation beneath the tip. Third, combined two-axis and three-axis misorientations are considered in order to assess interaction effects and identify the point at which the global responses begin to diverge more clearly.

We quantify these trends using three complementary observables: (i) the global load–displacement curve P–h, (ii) lattice-rotation maps extracted from the lattice-rotation tensor $\mathbf{R}$, and (iii) slip-system activity fields that identify changes in the dominant $\{110\}\langle 111\rangle$ systems. Where appropriate, asymmetry and sign changes are summarized using the scalar metrics introduced below.

In the present study, the imposed initial lattice misorientation is introduced by rotating the crystal frame while keeping the specimen geometry and indentation boundary conditions unchanged. The selected magnitudes of 2° and 5° are intended to represent small but plausible deviations from the nominal crystal orientation at the start of indentation. The smaller value is motivated by experimentally observed orientation offsets reported in the literature, whereas the larger value is used to probe the sensitivity of the response to a stronger, yet still moderate, crystallographic perturbation.

We first examine the global load–displacement response for the different misorientation cases. Fig. 6 shows that the P–h curves remain very similar for all cases, particularly for the 2° perturbations. Even for the 5° cases, the differences in maximum load remain small, and the responses can be grouped into only a few closely spaced levels. The cases $(0°, 0°, 0°)$ and $(0°, 0°, 5°)$ coincide at the highest load level, followed by $(5°, 0°, 0°)$ and $(5°, 0°, 5°)$, whereas $(0°, 5°, 0°)$ and $(0°, 5°, 5°)$ define a slightly lower group. These results indicate that the global indentation response is only weakly sensitive to small initial lattice misorientations, which helps explain why such effects are difficult to identify from load–displacement curves alone.

A different picture emerges from the lattice-rotation fields shown in Figs. 7 and 8, where even small initial lattice misorientations noticeably modify the symmetry, sign, and spatial extent of the subsurface rotation pattern. Among the single-axis cases, a non-zero θ_z produces a clear left–right asymmetry in the lattice-rotation field, whereas a non-zero θ_x promotes a pronounced sign change beneath the indenter tip. When these components are combined, as in $(5°, 0°, 5°)$, both effects are retained in the resulting field. Most combined cases follow this superposed behavior, although the $(5°, 5°, 0°)$ case shows that the interaction between components is not purely additive. The corresponding 2° cases exhibit the same qualitative trends, but with reduced magnitude. Overall, increasing the initial lattice misorientation broadens the rotation field and amplifies deviations from the aligned reference state.

These lattice-rotation trends are qualitatively consistent with the main experimental observations reported by Wang et al. [3], namely the appearance of asymmetry and sign changes in the subsurface orientation field beneath a wedge indent. The CPFEM results further clarify that such features can arise from small initial crystallographic offsets even when the corresponding global indentation curves remain nearly unchanged. Moreover, the rotation maps help interpret the small differences observed in the P–h curves: cases with more localized and symmetric rotation fields, such as $(0°, 0°, 0°)$ and $(0°, 0°, 5°)$, tend to show slightly higher maximum loads, whereas cases with broader rotation distributions tend to show slightly lower ones.

To further analyze these trends, the slip-system activity is examined using two complementary metrics: the accumulated plastic slip per slip-system and the slip rate at the end of loading. Together, these provide information on both the history-dependent hardening state and the final dominant slip activity. The resulting maps are shown in Figs. 9 and 10, where the dominant slip system in each element is identified from the largest value of the corresponding metric.

The slip-activity maps reinforce the trends already visible in the lattice-rotation fields. Cases with nearly identical P–h curves, such as $(0°, 0°, 0°)$ and $(0°, 0°, 5°)$, also show closely related spatial distributions of dominant slip activity. A non-zero θ_z component tends to introduce asymmetry about the centerline, while a non-zero θ_x component changes the dominant systems beneath the tip and is associated with the observed sign reversal in the lattice-rotation field. In particular, the comparison between $(0°, 0°, 0°)$ and $(5°, 0°, 0°)$ indicates that the sign change beneath the tip is accompanied by a change in the locally dominant slip systems. The cases involving θ_y retain a more symmetric distribution overall, but still exhibit noticeable redistribution of slip activity near the indenter tip and the free surfaces.

Comparing the cumulative-slip-based and slip-rate-based maps also highlights the distinction between the deformation history and the final active configuration. The two metrics show broadly consistent regional trends, but they do not always identify the same dominant slip system in a given location. This difference is expected: the slip-system strength reflects the integrated effect of prior hardening, whereas the slip rate characterizes the instantaneous response at the end of loading. Taken together, these results show that small initial lattice misorientations reorganize the local slip activity in a way that is much more evident in the subsurface fields than in the global indentation curve.

3.5. Quantification of asymmetry

During wedge nanoindentation, even small initial lattice misorientations can break the left–right symmetry of the subsurface deformation field and produce unequal lattice rotation on either side of the indenter. While this asymmetry is visually apparent in both simulated and

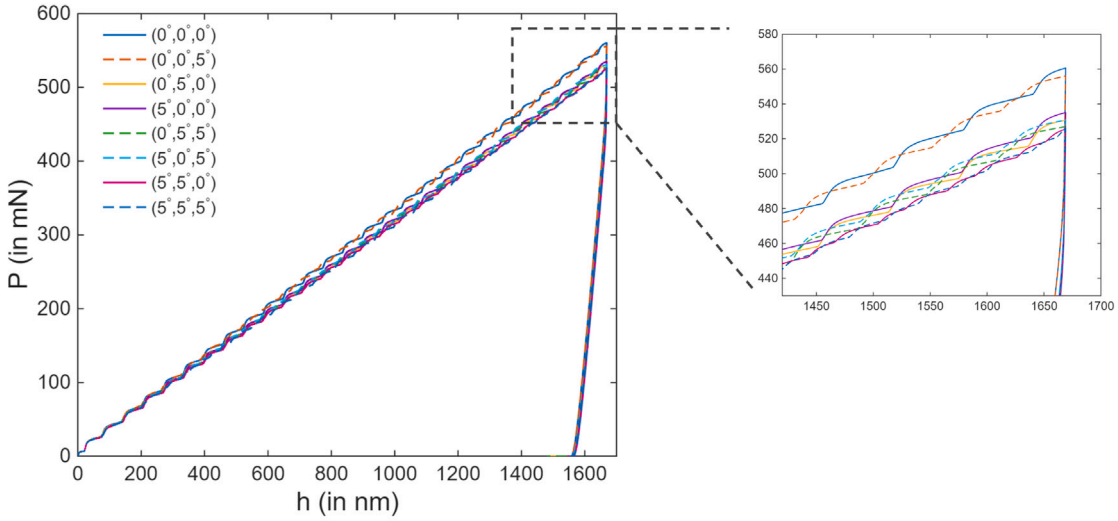

(a) Load–displacement response for cases with 5° initial lattice misorientation. The cases $(0°, 0°, 0°)$ and $(0°, 0°, 5°)$ coincide almost exactly, while $(5°, 0°, 0°)$ and $(5°, 0°, 5°)$ show slightly lower loads. The remaining cases form a closely grouped lower-response set.

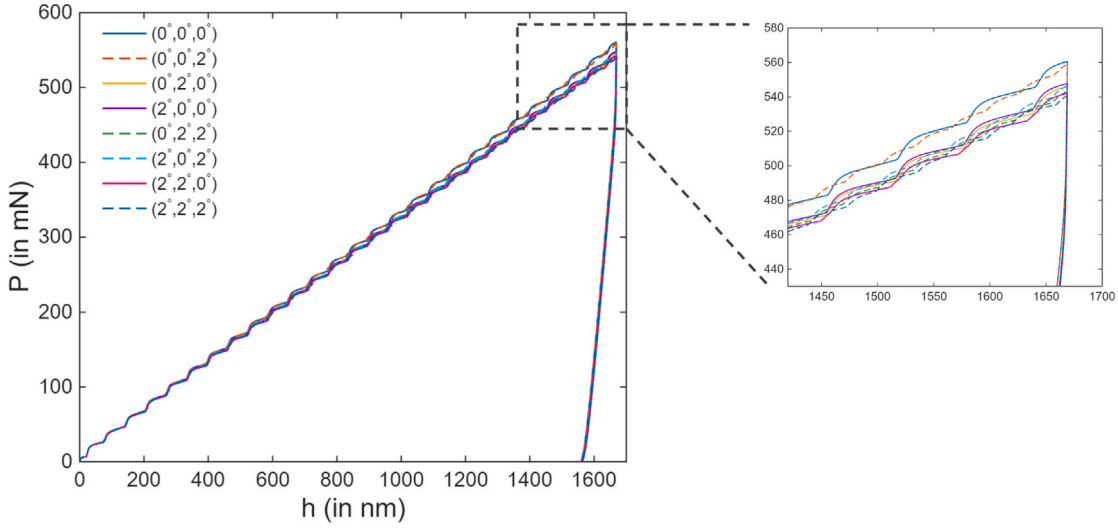

(b) Load–displacement response for cases with 2° initial lattice misorientation. The aligned case $(0°, 0°, 0°)$ and the $(0°, 0°, 2°)$ case coincide almost exactly, while the remaining cases also remain closely grouped, confirming the weak sensitivity of the global indentation response to small initial lattice misorientations.

Fig. 6. Effect of initial lattice misorientation on the load–displacement response during wedge nanoindentation of single-crystal tungsten. The aligned reference case and the misoriented cases remain closely grouped, indicating that the global indentation response is only weakly sensitive to small initial lattice misorientations.

experimental rotation maps, a scalar metric is useful for comparing its magnitude across different misorientation cases. For this purpose, we introduce an asymmetry index, denoted by $\mathcal{I}$, that quantifies the normalized difference in lattice rotation between symmetric positions about the indentation centerline. This index characterizes the deformation imbalance induced by the imposed crystallographic offset rather than the misorientation itself.

Building on this concept, an integral-based metric is defined directly from the lattice-rotation field obtained from the CPFEM simulations. Let $\theta(x, z)$ denote the lattice rotation in the x–z plane beneath the indenter. The continuous form of the asymmetry index is written as

$$\mathcal{I} = \frac{1}{A} \iint_{\Omega_{x>0}} \frac{|\theta(x,z) - \theta(-x,z)|}{|\theta(x,z)| + |\theta(-x,z)|} \, \mathrm{d}A, \tag{18}$$

where A is the projected area of the analyzed half-domain, $\Omega_{x>0}$.

In the discrete CPFEM implementation, $\theta(x, z)$ is evaluated at the centroids of finite elements. Symmetric element pairs located at (x_i, z_i) and $(-x_i, z_i)$ are compared using the local contribution

$$I_i = \frac{|R_i - L_i|}{|R_i| + |L_i| + \varepsilon}, \tag{19}$$

where $R_i = \theta(x_i, z_i)$, $L_i = \theta(-x_i, z_i)$, and ε is a small regularization parameter introduced to avoid division by zero. The global asymmetry index is then obtained as

$$\mathcal{I} = \frac{1}{N} \sum_{i=1}^{N} I_i, \tag{20}$$

where N is the total number of symmetric element pairs considered in the analysis. Because the mesh is uniform in the present study and the deformation nearly isochoric, no additional area weighting is required in the discrete summation.

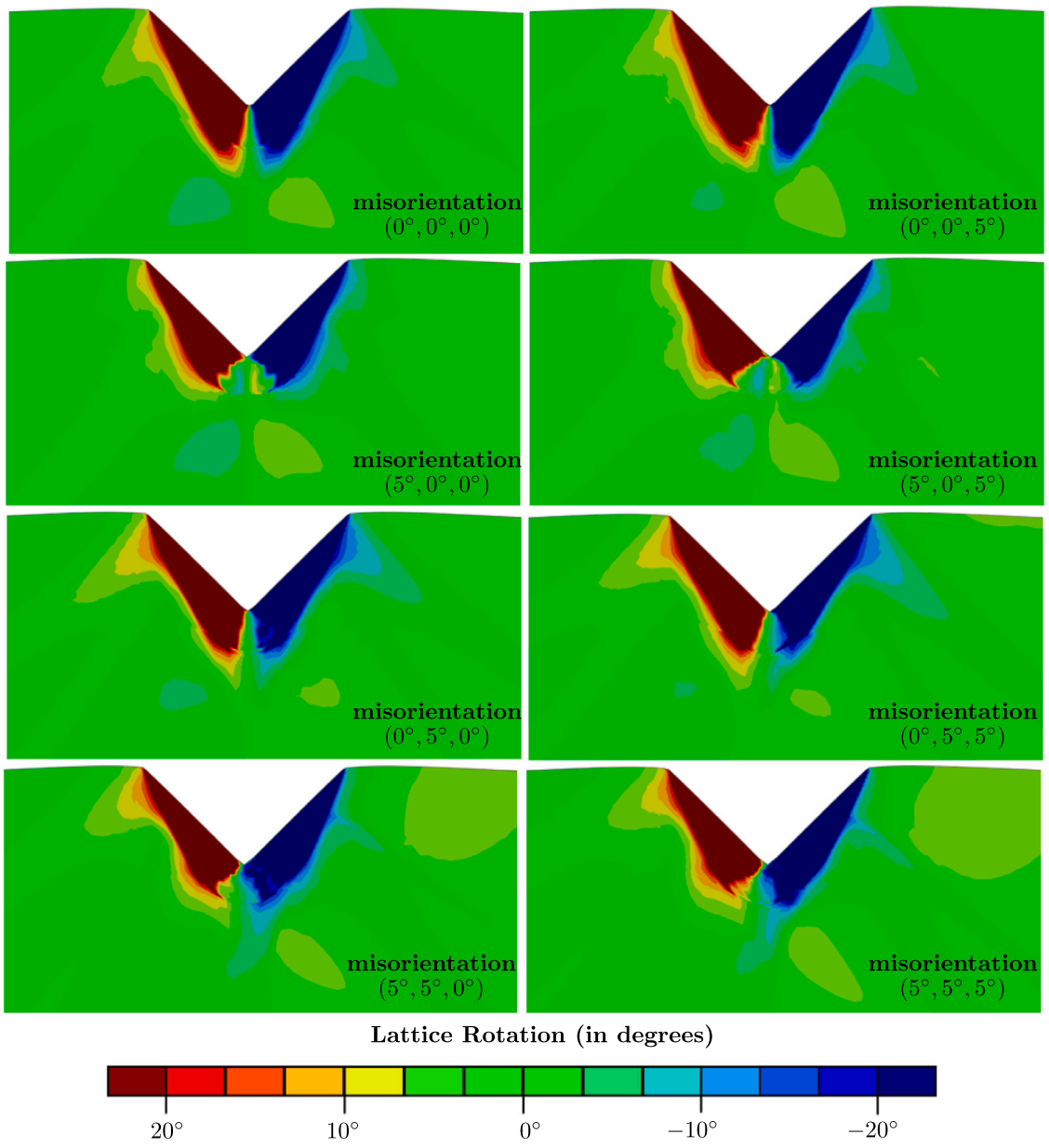

Fig. 7. Lattice-rotation fields at maximum indentation depth for cases with 5° initial lattice misorientation. The imposed rotation components are indicated in each panel as $(\theta_x, \theta_y, \theta_z)$. Small changes in the initial crystal orientation produce pronounced differences in the symmetry, sign, and spatial extent of the subsurface lattice-rotation pattern.

Fig. 11 shows that the asymmetry index increases systematically with initial lattice misorientation, but the rate of increase depends strongly on the rotation axis. Among the single-axis cases, $(0°, 0°, \theta)$ produces by far the largest asymmetry, whereas $(\theta, 0°, 0°)$ and $(0°, \theta, 0°)$ contribute only weakly over the range considered. This confirms that the z-component is the dominant driver of left–right symmetry breaking in the lattice-rotation field.

For combined rotations, the response is not simply additive. The pair $(\theta, 0°, \theta)$ consistently generates the largest asymmetry among the two-axis cases, exceeding both the single-axis $(0°, 0°, \theta)$ case and the other two-axis combinations. By contrast, $(\theta, \theta, 0°)$ and $(0°, \theta, \theta)$ remain lower and change their relative ordering as θ increases, indicating that interactions between the rotation components become increasingly nonlinear at larger angular magnitudes.

The three-axis case (θ, θ, θ) further illustrates this nonlinear behavior. At low misorientation magnitudes, its asymmetry index exceeds that of $(\theta, 0°, \theta)$, whereas at $\theta = 10°$ it falls below both $(\theta, 0°, \theta)$ and the single-axis $(0°, 0°, \theta)$ response. This decrease indicates that the contribution of the individual rotation components is not additive. Rather than producing a monotonic increase in asymmetry, the combined rotations lead to a progressively more complex lattice-rotation response, consistent with the trends already observed between the $(0°, 0°, \theta)$, $(\theta, 0°, \theta)$, and (θ, θ, θ) cases at lower misorientation magnitudes. The comparison between $(5°, 5°, 5°)$ and $(5°, 5°, -5°)$ further supports this interpretation, since reversing the sign of the z-component significantly increases

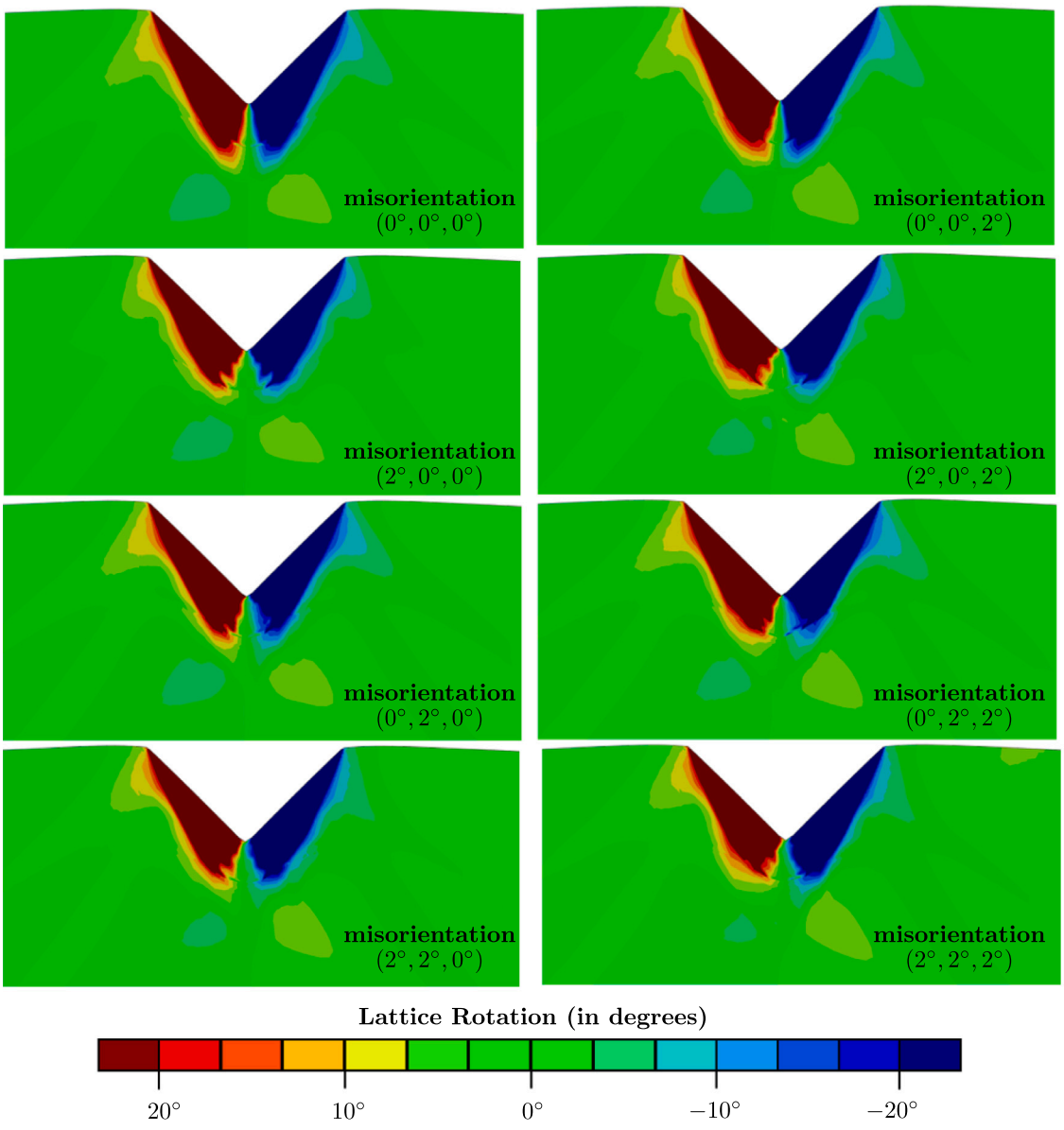

Fig. 8. Lattice-rotation fields at maximum indentation depth for cases with 2° initial lattice misorientation. The same qualitative trends observed for the 5° cases are retained, but with reduced magnitude, confirming that even small crystallographic offsets can modify the local deformation field.

the asymmetry. This observation highlights the dominant influence of the loading-axis rotation while simultaneously demonstrating that the interaction between the individual rotation components remains strongly nonlinear.

A small nonzero value of $\mathcal{I}$ is also obtained for the nominally aligned case $(0°, 0°, 0°)$; this residual level is attributed to numerical error in the finite element solution and post-processing, and is therefore treated as the baseline offset of the metric.

4. Summary and conclusions

In this study, a plane-strain crystal plasticity finite element model of 90° wedge nanoindentation was developed for body-centered-cubic single-crystal tungsten and calibrated against the experimental load–displacement response reported by Wang et al. [3]. The calibrated model was then used to investigate how small initial lattice misorientations affect the global indentation response, the subsurface lattice-rotation field, and the spatial distribution of slip activity beneath the indenter.

The simulations show that small initial lattice misorientations have only a limited influence on the global load–displacement response, but substantially modify the local deformation pattern. In particular, the lattice-rotation field becomes increasingly asymmetric as the imposed misorientation increases, and the dominant slip activity changes depending on both the rotation axis and the rotation magnitude. Among the single-axis cases, the Z-component is the dominant driver of left–right asymmetry in the lattice-rotation field, whereas the X-component is associated with a sign reversal of lattice rotation beneath the indenter tip. These local-field trends are consistent with the experimentally observed asymmetry of subsurface orientation maps and help explain

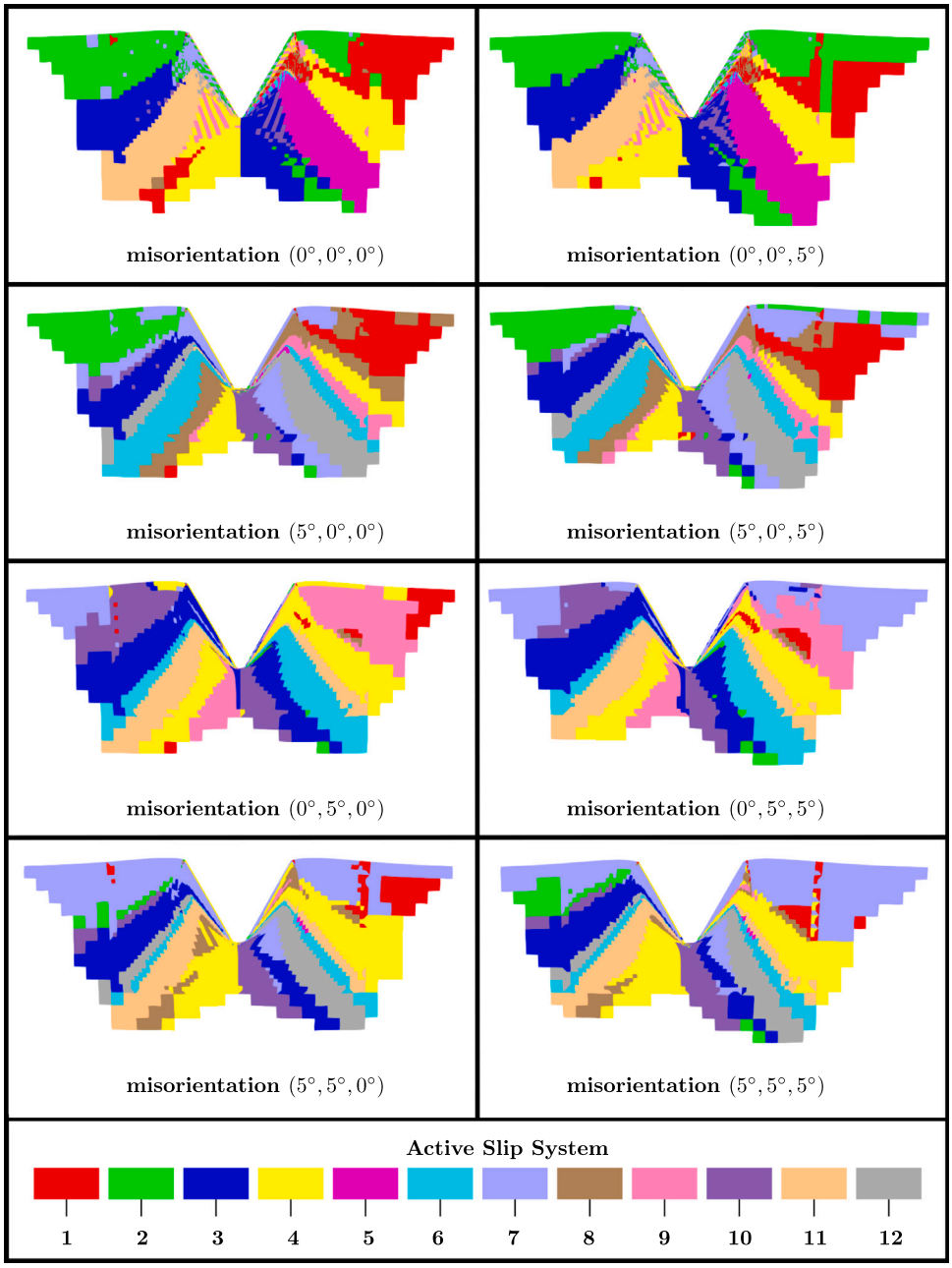

Fig. 9. Slip-system activity mapped using the accumulated plastic slip on each slip-system at the end of indentation. In each element, the color denotes the dominant slip system within the active $\{110\}\langle 111\rangle$ family. For the $(0°, 0°, 0°)$ and $(0°, 0°, 5°)$ cases, two jointly dominant systems are identified in some regions; for the remaining cases, a single dominant system is observed in each region. The imposed initial lattice misorientation $(\theta_x, \theta_y, \theta_z)$ is indicated in each panel. (For interpretation of the references to color in this figure legend, the reader is referred to the web version of this article.)

why pronounced differences in local deformation may coexist with only small changes in the corresponding indentation curves.

From a constitutive perspective, the calibration study further shows that the global response is highly sensitive to the assumed slip-family description. In the present configuration, models with three active BCC slip families remain too soft to reproduce the experimental loading response within a physically reasonable parameter range, whereas the reduced $\{110\}\langle 111\rangle$ formulation provides sufficient sensitivity to the constitutive parameters and yields good agreement with the measured response. This choice is further supported by the broader BCC slip literature. Weinberger et al. [27] reviewed experimental and atomistic evidence across BCC transition metals and highlighted that slip in tungsten is frequently associated with $\{110\}$ planes, although activity on $\{112\}$ planes has also been reported under certain conditions. The same review further notes that many atomistic studies identify $\{110\}$ as the fundamental slip plane governing screw-dislocation motion in BCC tungsten. The present model should therefore be interpreted as an effective reduced-order description of the room-temperature slip response governing the indentation experiments considered here.

The main findings of the study can be summarized as follows:

- Small initial lattice misorientations produce only minor changes in the global load–displacement response. Relative to the aligned

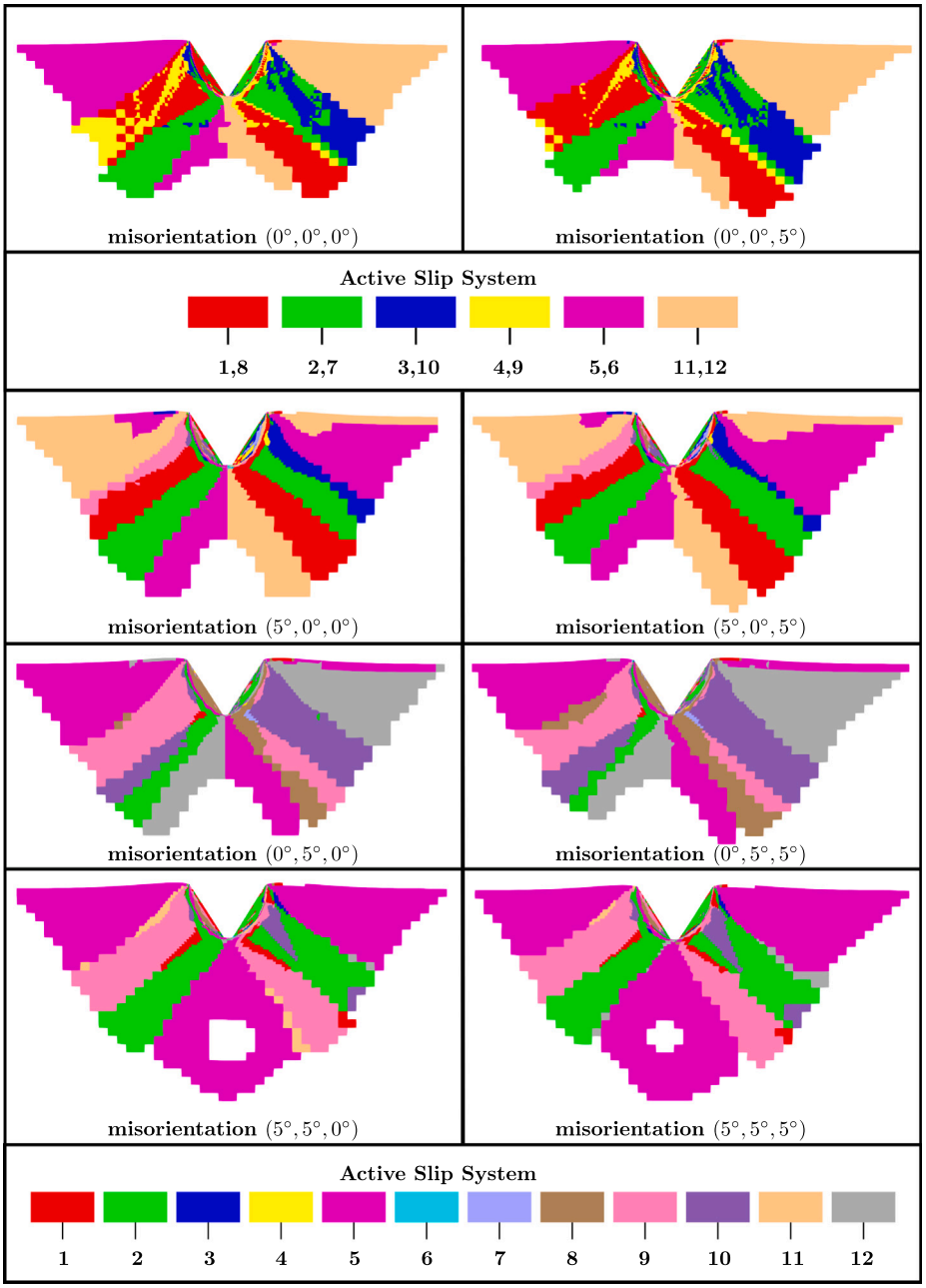

Fig. 10. Slip-system activity mapped using the slip rate at the end of indentation. In each element, the color denotes the dominant active slip system within the $\{110\}\langle 111\rangle$ family. The $(0°, 0°, 0°)$ and $(0°, 0°, 5°)$ cases show regions with two jointly dominant systems, whereas the remaining cases are characterized by a single dominant system in each region. The imposed initial lattice misorientation $(\theta_x, \theta_y, \theta_z)$ is indicated in each panel. (For interpretation of the references to color in this figure legend, the reader is referred to the web version of this article.)

reference case, the maximum indentation load decreases by approximately 3.6% for the 2° misorientation cases and by up to approximately 5.4% for the 5° cases.

- Local observables, including lattice rotation and slip activity, are substantially more sensitive to initial lattice misorientation than the global indentation curve alone. In particular, the asymmetry index increases from the residual reference value of $I = 0.0121$ for the aligned configuration to approximately $I = 0.3$–0.4 for the 5° misorientation cases, with rotations involving the Z-component producing the strongest asymmetry. Thus, while the global indentation response varies only by a few percent, the local asymmetry measure increases by more than an order of magnitude relative to the aligned reference state.
- A nonzero X-component is associated with a sign reversal of lattice rotation beneath the indenter tip and with a redistribution of the locally dominant slip systems.
- Increasing the magnitude of the initial lattice misorientation broadens the lattice-rotation field and enhances deviations from the aligned reference state.
- The slip-system activity maps derived from accumulated plastic slip and final slip rate reveal consistent regional trends while

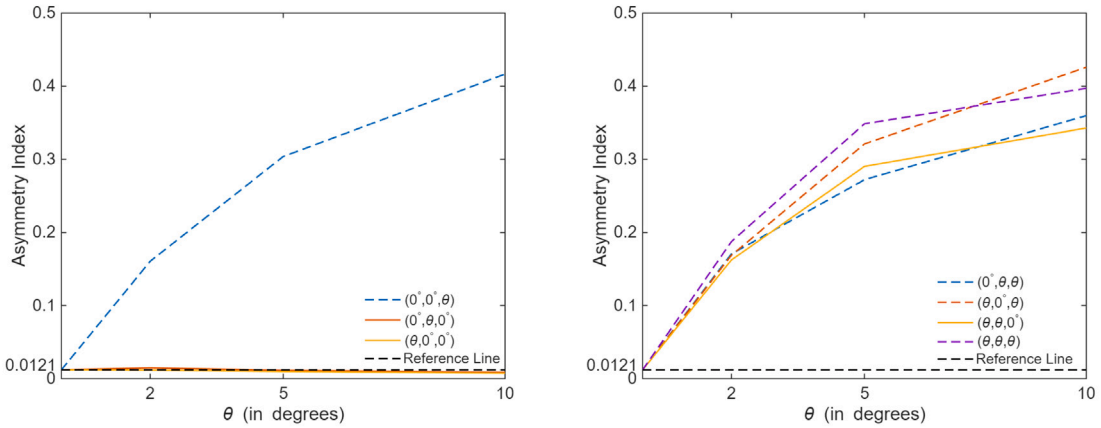

(a) Single-axis misorientation. (b) Multi-axis misorientation.

Fig. 11. Asymmetry index $\mathcal{I}$ as a function of initial lattice misorientation for (a) single-axis rotations $(\theta, 0°, 0°)$, $(0°, \theta, 0°)$, and $(0°, 0°, \theta)$, and (b) combined rotations $(\theta, \theta, 0°)$, $(\theta, 0°, \theta)$, $(0°, \theta, \theta)$, and (θ, θ, θ). Rotation about the z-axis is the dominant contributor to asymmetry, while multi-axis cases show nonlinear interactions that may either amplify or partially compensate the net deformation imbalance.

highlighting the distinction between cumulative deformation history and the instantaneous active configuration.

Overall, the present analysis shows that local deformation fields beneath a wedge indenter provide a far more sensitive indication of the initial crystallographic state than the global indentation response. For wedge nanoindentation in single-crystal tungsten, reliable interpretation of experimentally measured subsurface orientation fields therefore requires careful consideration of small initial lattice misorientations. More broadly, the study demonstrates how CPFEM-based lattice-rotation analysis can be used to link orientation-sensitive measurements with their underlying micromechanical origins in anisotropic crystalline materials.

CRediT authorship contribution statement

T.O. Fenercioğlu: Writing – original draft, Visualization, Methodology, Formal analysis, Conceptualization. **M. Budnitzki:** Writing – original draft, Validation, Supervision, Methodology, Investigation, Conceptualization. **J. Wang:** Visualization, Data curation. **S. Sandfeld:** Supervision. **R. Schwaiger:** Supervision.

Declaration of competing interest

The authors declare that they have no known competing financial interests or personal relationships that could have appeared to influence the work reported in this paper.

Appendix A. Pseudocode for lattice rotation calculation

The following pseudocode illustrates the extraction of Bunge-convention Euler angles from a given lattice rotation matrix. A numerical tolerance of $\epsilon = 10^{-3}$ is introduced to ensure robust extraction of Bunge-convention Euler angles from the lattice-rotation matrix. This tolerance reduces the influence of numerical noise and floating-point roundoff in the trigonometric evaluation, particularly near singular cases where $\phi \approx 0$ or $\phi \approx \pi$. The selected threshold was verified by applying known rigid rotations to an initial cubic orientation and confirming that the recovered Euler angles remained consistent with the imposed lattice rotation.

Algorithm 1 Extraction of Bunge Euler angles from the lattice-rotation matrix.

$\epsilon \leftarrow 10^{-3}$ ▷ Numerical tolerance
$\phi \leftarrow \arccos(R_{33})$
if $\phi < \epsilon$ **then**
  $\varphi_1 \leftarrow \arctan 2(-R_{21}, R_{11})$
  $\varphi_2 \leftarrow 0$
else if $|\pi - \phi| < \epsilon$ **then**
  $\varphi_1 \leftarrow \arctan 2(R_{21}, R_{11})$
  $\varphi_2 \leftarrow 0$
else
  $\varphi_1 \leftarrow \arctan 2(R_{31}, -R_{32})$
  $\varphi_2 \leftarrow \arctan 2(R_{13}, R_{23})$
end if
if $\varphi_1 < 0$ **then**
  $\varphi_1 \leftarrow \varphi_1 + 2\pi$
end if
if $\varphi_2 < 0$ **then**
  $\varphi_2 \leftarrow \varphi_2 + 2\pi$
end if

Appendix B. Implementation of experimental displacement rate

An initial implementation prescribed a constant displacement rate corresponding to a total indentation depth of 1656 nm applied over a unit step time. Because the CPFEM formulation used in this study is rate dependent, this idealized loading history was replaced by the experimentally measured displacement–time curve in order to represent the actual loading path more faithfully (Fig. B.12a).

Direct use of the raw experimental signal led to convergence difficulties in the finite element simulations. These instabilities were traced to local fluctuations in the measured displacement history, which produced non-monotonic segments and therefore implied short intervals of apparent indenter retraction during loading. To regularize the boundary condition, the displacement history was differentiated to obtain the corresponding velocity profile (Fig. B.12b), and the resulting signal was smoothed and corrected to ensure a strictly positive indentation velocity throughout the loading step.

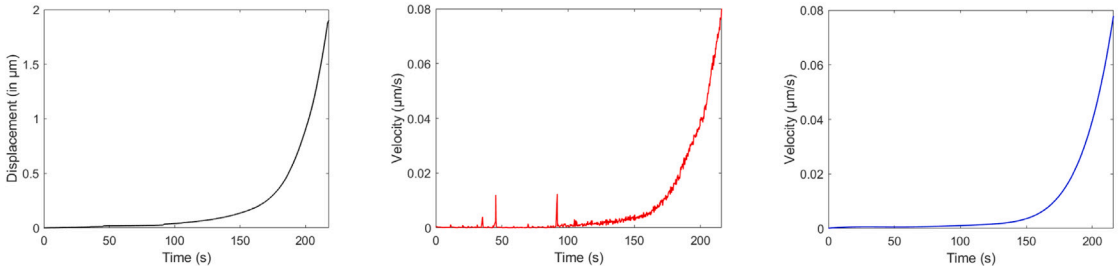

(a) Experimental displacement–time curve. (b) Raw velocity profile from differentiation. (c) Smoothed velocity used in simulation.

Fig. B.12. Processing of the experimental loading history used in the CPFEM simulations: (a) measured displacement–time input, (b) raw velocity profile obtained by differentiation, and (c) smoothed velocity history prescribed as the numerical boundary condition.

The processed experimental data were fitted using a sixth-order polynomial regression model implemented in MATLAB's Curve Fitting Toolbox (MATLAB R2024b; [28]). The fitted velocity history was then prescribed as the boundary condition in the CPFEM simulations (Fig. B.12c). This treatment improved numerical stability and required a recalibration of the constitutive parameters, since the predicted load–displacement response differed slightly from that obtained under constant-velocity loading. Despite the adjustment in the fitted parameters, the predicted lattice-rotation fields and dominant slip-system distributions remained effectively unchanged, indicating that the mechanistic interpretation of the results is robust with respect to the loading-history correction.

Data availability

Data will be made available on request.

References

[1] W.C. Oliver, G.M. Pharr, Measurement of hardness and elastic modulus by instrumented indentation: Advances in understanding and refinements to methodology, J. Mater. Res. (2004) 3–20.

[2] George M. Pharr, Erik G. Herbert, Yanfei Gao, The indentation size effect: A critical examination of experimental observations and mechanistic interpretations, Annu. Rev. Mater. Res. (2010) 271–292.

[3] Jin Wang, Tillmann Volz, Sabine M. Weygand, Ruth Schwaiger, The indentation size effect of single-crystalline tungsten revisited, J. Mater. Res. (2021) 2166–2175.

[4] W.C. Oliver, G.M. Pharr, An improved technique for determining hardness and elastic modulus using load and displacement sensing indentation experiments, J. Mater. Res. (1992) 1564–1583.

[5] G.M. Pharr, W.C. Oliver, F.R. Brotzen, On the generality of the relationship among contact stiffness, contact area, and elastic modulus during indentation, J. Mater. Res. (1992) 613–617.

[6] C.G.N. Pelletier, E.C.A. Dekkers, L.E. Govaert, J.M.J. Toonder, H.E.H. Meijer, The influence of indenter-surface misalignment on the results of instrumented indentation tests, Polym. Test. (2007) 949–959.

[7] Naureen B. Shahjahan, Zhong Hu, Effects of angular misalignment on material property characterization by nanoindentation with a cylindrical flat-tip indenter, J. Mater. Res. (2016) 1456–1465.

[8] Chengli Shi, Hongwei Zhao, Hu Huang, Lixia Xu, Luquan Ren, Meilin Bai, Jianping Li, Xiaoli Hu, Effects of indenter tilt on nanoindentation results of fused silica: an investigation by finite element analysis, Mater. Trans. (2012) 958–963.

[9] Mahdi Saket Kashani, Sources of Error in Relating Nanoindentation Results to Material Properties (Ph.d. thesis), Wichita State University, College of Engineering, Wichita, 2010.

[10] N. Zaafarani, D. Raabe, R.N. Singh, F. Roters, S. Zaefferer, Three-dimensional investigation of the texture and microstructure below a nanoindent in a Cu single crystal using 3D EBSD and crystal plasticity finite element simulations, Acta Mater. (2006) 1863–1876.

[11] J.W. Kysar, Y. Saito, M.S. Oztop, D. Lee, W.T. Huh, Experimental lower bounds on geometrically necessary dislocation density, Int. J. Plast. (2010) 1097–1123.

[12] J. Lynggaard, K.L. Nielsen, C.F. Niordson, Finite strain analysis of size effects in wedge indentation into a Face-Centered Cubic (FCC) single crystal, Eur. J. Mech. A Solids (2019) 193–207.

[13] Yonggang Huang, A User-Material Subroutine Incorporating Single Crystal Plasticity in the ABAQUS Finite Element Program (PhD thesis), Harvard University, 1991.

[14] Michael Smith, ABAQUS/Standard User's Manual, Version 6.9, Dassault Systèmes Simulia Corp, United States, 2009.

[15] R. Hill, Generalized constitutive relations for incremental deformation of metal crystals by multislip, J. Mech. Phys. Solids (1966) 95–102.

[16] E.H. Lee, Elastic-plastic deformation at finite strains, ASME J. Appl. Mech. (1969) 1–6.

[17] J.R. Rice, Inelastic constitutive relations for solids: An internal-variable theory and its application to metal plasticity, J. Mech. Phys. Solids (1971) 433–455.

[18] R. Hill, J.R. Rice, Constitutive analysis of elastic-plastic crystals at arbitrary strain, J. Mech. Phys. Solids (1972) 401–413.

[19] D. Peirce, R.J. Asaro, A. Needleman, An analysis of nonuniform and localized deformation in ductile single crystals, Acta Metall. 30 (6) (1982) 1087–1119.

[20] Dorian Depriester, Computing Euler angles with Bunge convention from rotation matrix, 2018, http://dx.doi.org/10.13140/RG.2.2.34498.48321/5, Available online.

[21] W.Z. Yao, J.H. You, Berkovich nanoindentation study of monocrystalline tungsten: a crystal plasticity study of surface pile-up deformation, Phil. Mag. 97 (17) (2017) 1418–1435, http://dx.doi.org/10.1080/14786435.2017.1299237.

[22] M.J. Lewandowski, S. Stupkiewicz, Size effects in wedge indentation predicted by a gradient-enhanced crystal-plasticity model, Int. J. Plast. (ISSN: 0749-6419) 109 (2018) 54–78, http://dx.doi.org/10.1016/j.ijplas.2018.05.008, URL https://www.sciencedirect.com/science/article/pii/S0749641918301384.

[23] Yue-Lin Liu, Hong-Bo Zhou, Ying Zhang, Shuo Jin, Guang-Hong Lu, The ideal tensile strength and deformation behavior of a tungsten single crystal, Nucl. Instrum. Methods Phys. Res. Sect. B: Beam Interact. Mater. Atoms 267 (18) (2009) 3282–3285.

[24] Tillmann Volz, Deformation Behavior of Tungsten Single Crystals During Wedge Nanoindentation - A Numerical Study (Phd thesis), Karlsruher Institut für Technologie (KIT), 2020.

[25] Daniel N. Blaschke, Averaging of Elastic Constants for Polycrystals, Technical Report LA-UR-17-24288, Los Alamos National Laboratory, 2017, URL https://arxiv.org/abs/1706.07132, Los Alamos National Laboratory Report, September 2017.

[26] Jaroslav Menčík, Uncertainties and errors in nanoindentation, in: Jiri Nemecek (Ed.), Nanoindentation in Materials Science, InTech, 2012, p. 322, Available online.

[27] C.R. Weinberger, B.L. Boyce, C.C. Battaile, Slip planes in bcc transition metals, Int. Mater. Rev. 58 (5) (2013) 296–314, http://dx.doi.org/10.1179/1743280412Y.0000000015.

[28] The MathWorks Inc., Curve fitting toolbox, 2020, URL https://www.mathworks.com/products/curvefitting.html.